In vivo near-infrared fluorescence imaging of osteoblastic activity

Article *in* Nature Biotechnology · January 2002

DOI: 10.1038/nbt1201-1148 · Source: OAI

6 authors, including:

Robert Lenkinski
University of Texas Southwestern Medical Center
370 PUBLICATIONS **16,102** CITATIONS

SEE PROFILE

Lewis C Cantley
Harvard University
795 PUBLICATIONS **157,857** CITATIONS

SEE PROFILE

In vivo near-infrared fluorescence imaging of osteoblastic activity

Atif Zaheer[1], Robert E. Lenkinski[1], Ashfaq Mahmood[2], Alun G. Jones[2], Lewis C. Cantley[3], and John V. Frangioni[4]*

In vertebrates, the development and integrity of the skeleton requires hydroxyapatite (HA) deposition by osteoblasts. HA deposition is also a marker of, or a participant in, processes as diverse as cancer and atherosclerosis. At present, sites of osteoblastic activity can only be imaged *in vivo* using γ-emitting radioisotopes. The scan times required are long, and the resultant radioscintigraphic images suffer from relatively low resolution. We have synthesized a near-infrared (NIR) fluorescent bisphosphonate derivative that exhibits rapid and specific binding to HA *in vitro* and *in vivo*. We demonstrate NIR light–based detection of osteoblastic activity in the living animal, and discuss how this technology can be used to study skeletal development, osteoblastic metastasis, coronary atherosclerosis, and other human diseases.

The development and maintenance of the vertebral skeleton represents a balance between osteoblast-induced mineralization and osteoclast-induced demineralization (reviewed in ref. 1). Osteoblast-like cells are also present in the vascular wall and participate in the earliest manifestations of atherosclerosis (reviewed in refs 2,3). HA is the major mineral product of osteoblasts and calcifying vascular cells, and binds naturally occurring pyrophosphates and phosphonates with high affinity[4].

Bisphosphonates are synthetic phosphonate derivatives in which the canonical P-O-P bond is replaced by a nonhydrolyzable P-C-P bond (reviewed in ref. 5). Through direct and indirect effects, bisphosphonates inhibit osteoclast function and hence shift the balance toward HA deposition. Clinically, bisphosphonates are prescribed widely as an effective treatment for osteoporosis (reviewed in refs 6,7) and complications from certain malignancies (reviewed in ref. 8). Bisphosphonates can also be used as carriers for other functional groups[9–15]. Clinical bone scans, for example, utilize technetium-99m (^{99m}Tc)-methylene diphosphonate (MDP) injected intravenously. The 140 keV γ-ray emitted from ^{99m}Tc is imaged with planar γ/SPECT cameras after localization in the bone.

Currently, there exists no nonisotopic method for directly detecting osteoblastic activity *in vivo*. In the ultraviolet and visible ranges, bone exhibits high absorbance and autofluorescence[16,17], and photon scatter is high. In general, biological tissue exhibits a high photon absorbance in both the visible wavelength range (350–700 nm; secondary to hemoglobin, tissue pigments, etc.) and in the infrared range (>900 nm; secondary to lipids and water). However, in the NIR "window" from 700 nm to 900 nm (ref. 18), the absorbance spectra for all biomolecules reach minima. Hence, NIR fluorescent light for the detection of HA has several inherent advantages. First, photon penetration into, and out of, tissue is high. Second, tissue absorption and autofluorescence is minimized, yielding an inherently high contrast between target and background. Third, optical scatter within tissue is lower.

We have synthesized a NIR fluorescent bisphosphonate derivative with nearly ideal optical and HA-binding properties. We report the NIR fluorescence imaging of a complete body system, the growing skeleton, in a living animal. We compare NIR fluorescence imaging with ^{99m}Tc-MDP radioscintigraphy and magnetic resonance imaging (MRI) in the same animal, and discuss technical advantages and limitations of these imaging modalities. Finally, we suggest how this technology can be used to study skeletal development, genetic changes associated with osteoblastic metastases, and early calcification in atherosclerosis.

Results

Conjugation and purification of Pam78. We chose pamidronate (Fig. 1A, molecule I) for this study because it has a single primary amine for conjugation, is available in powder form, and has a short spacing element (two carbons). After covalent conjugation to the *N*-hydroxysuccinimide (NHS) ester of the NIR fluorophore IRDye78 (Fig. 1A, molecule II; see Experimental Protocol), the resultant product, termed Pam78 (Fig. 1A, molecule III), was purified using thin-layer chromatography (TLC; Fig. 1B) and confirmed by mass spectroscopy (data not shown). Because of pamidronate's extreme insolubility in organic solvents and IRDye78's base lability, we carried out the conjugation reaction in aqueous solution, with typical Pam78 yields of 18–21%.

Spectral properties of IRDye78 and Pam78. Both IRDye78 (Fig. 1C, left panel) and Pam78 (Fig. 1C, right panel) had peak absorption at 771 nm, with a minor peak at 708 nm (discussed below). Emission fluorescence scans revealed peak emission for both fluorophores at 796 nm (Fig. 1D). Notably, excitation at the minor absorption peak of 708 nm resulted in identical peak emission wavelengths for both IRDye78 and Pam78 (data not shown), indicating that this minor absorption peak is an alternative resonance structure and not an impurity in the preparation. Conjugation to pamidronate probably stabilizes this alternative resonance.

***In vitro* HA-binding properties.** In a kinetic binding assay (Fig. 2A), Pam78 exhibited rapid binding to HA, with 37% of peak

[1]*Department of Radiology, Beth Israel Deaconess Medical Center, Boston, MA 02215.* [2]*Department of Radiology, Brigham and Women's Hospital and Harvard Medical School, Boston, MA, 02115. Divisions of* [3]*Signal Transduction and* [4]*Hematology/Oncology, Department of Medicine, Beth Israel Deaconess Medical Center, Boston, MA 02215. *Corresponding author (jfrangio@caregroup.harvard.edu).*

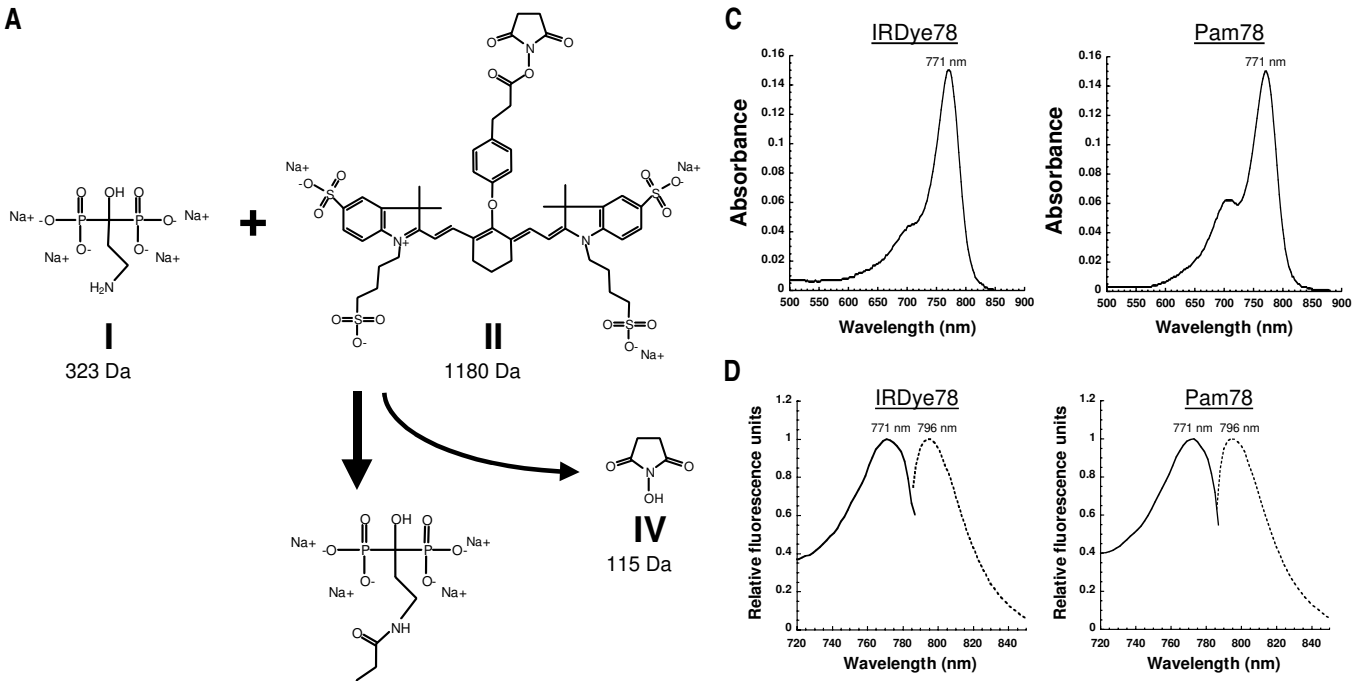

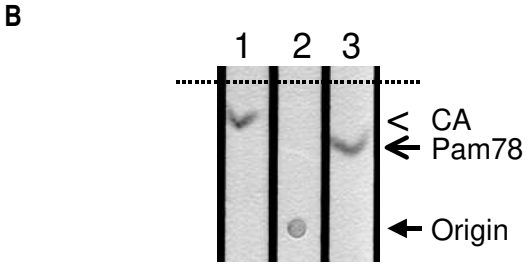

Figure 1. Conjugation of pamidronate to IRDye78, purification of the product, and spectral characteristics. (A) The primary amine of pamidronate tetrasodium (**I**) was conjugated to the sodium salt of the *N*-hydroxysuccinimide (NHS) ester of IRDye78 (**II**), as described in the Experimental Protocol, yielding the NIR fluorescent product pamidronate/IRDye78 (**III**; Pam78) and *N*-hydroxysuccinimide (**IV**). The chemical structure and molecular mass (in daltons) for each compound are shown. The carboxylic acid of IRDye78 is compound **I** with a hydrogen replacing the succinimide group. (B) Representative TLC separation of the reactants and products of the chemical reaction described in (A). The carboxylic acid of IRDye78 (lane 1, arrowhead), free pamidronate (lane 2, closed arrow; visualized with ninhydrin), and Pam78 (lane 3, open arrow) separated with R_f values of 0.8, 0, and 0.6, respectively. The origin is indicated, and the mobile-phase front is shown across the top of the plate as a dashed line. (C) Absorbance wavelength scans using IRDye78 (left panel) and Pam78 (right panel) at a concentration of 1 μM in NK buffer. The wavelength of peak absorption is indicated. (D) Excitation/emission fluorescence wavelength scans using IRDye78 (left panel) and Pam78 (right panel) at a concentration of 500 nM in NK buffer. For fluorescence excitation scans (solid lines), emission wavelength was fixed at 796 nm. For fluorescence emission scans (dashed lines), excitation wavelength was fixed at 771 nm. The peak wavelength for each scan is shown above the corresponding curve.

binding achieved in 5 min and asymptotic binding by 1 h. The carboxylic acid of IRDye78 (Fig. 2A) exhibited no detectable binding to HA.

To determine whether the capacity of HA to bind pamidronate was altered by conjugation to IRDye78, we measured binding as a function of applied bisphosphonate concentration (Fig. 2B). The observed binding was lower than previously published results for similar, but unconjugated, bisphosphonates[4] by a ratio exactly equal to the ratio of their respective molecular weights. This suggests that binding to HA was unaltered by conjugation, but that the total capacity of binding was lowered by steric hindrance.

Designed as pyrophosphate mimetics, bisphosphonates have extremely high specificity for HA both *in vitro*[4] and *in vivo*[19]. Nevertheless, we sought to confirm that Pam78 binding to HA could be competed by unlabeled pamidronate. Figure 2C shows the results of such a competition experiment. Theoretical estimates suggest that HA has a maximum binding capacity of ~8.4×10^{-4} mol pamidronate per g HA. Hence, the HA in each 100 μl reaction would be expected to have a capacity of 126 nmol of pamidronate. As shown in Figure 2C, Pam78 was effectively competed by increasing concentrations of unlabeled pamidronate, with 90% inhibition seen in the presence of 80 nmol (800 μM) unlabeled pamidronate.

***In vivo* NIR fluorescence imaging.** The small-animal imaging system we used is similar to one published previously[20]. It has an adjustable circular field of view (FOV) with a theoretical and measured resolution, respectively, of 100 μm and 200 μm at a FOV diameter of 10 cm, and 10 μm and 25 μm at a FOV diameter of 1 cm. The fluorescence excitation power density of the system was 18 mW/cm^2, with minimal spatial variation.

Because body hair causes significant light scatter and essentially precludes planar NIR imaging of small animals (see also below), we used hairless (*nu*/*nu*) mice. Figure 3A shows a typical experiment using the carboxylic acid of IRDye78 injected intravenously. NIR autofluorescence of the animal was negligible (Fig. 3A, B). Within 1 min, and appearing relatively stable for the next 15 min,

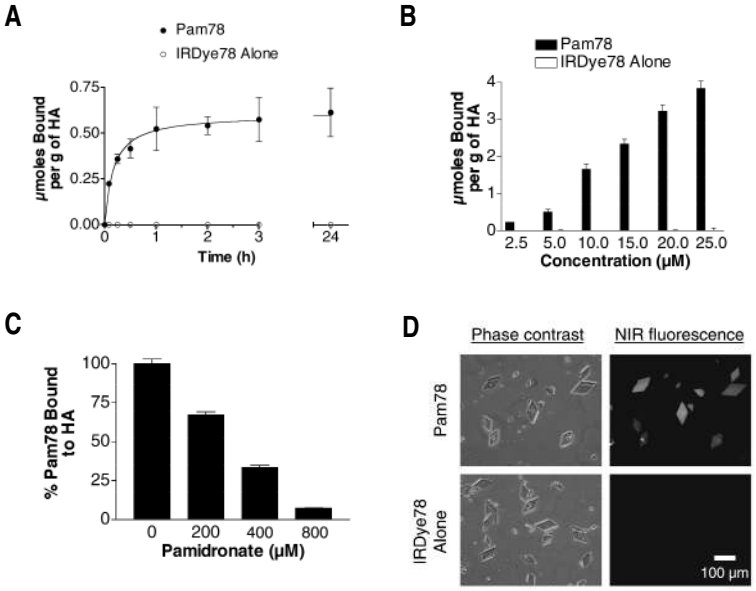

Figure 2. HA-binding properties of IRDye78 and Pam78. (A) The kinetics of binding to HA crystals was measured for Pam78 (solid circles) and the carboxylic acid of IRDye78 (IRDye78 alone; open circles). Measurements were acquired at 5, 15, and 30 min, and 1, 2, 3, and 24 h after mixing. Ordinate, µmoles of each compound bound per gram of HA (mean ± s.e.m.). (B) Steady-state binding to HA crystals was measured for Pam78 (solid bars) and the carboxylic acid of IRDye78 (IRDye78 alone; open bars). Abscissa, concentration of applied compound. Ordinate, µmoles of each compound bound per gram of HA (mean ± s.e.m.) at 3 h. (C) Competition of Pam78 binding to HA using unlabeled pamidronate. Ordinate, µmoles of each compound bound per gram of HA (mean ± s.e.m.) relative to binding of Pam78 in the absence of unlabeled pamidronate. (D) Direct visualization of Pam78 binding to HA using NIR fluorescence microscopy. Phase contrast (left panels) and NIR fluorescence images (right panels) of HA crystals treated with 1 µM Pam78 (top panels) or the carboxylic acid of IRDye78 (bottom panels) are shown.

the entire mouse became fluorescent (Fig. 3A). Notably, any small defects present on the animal's skin became pronounced after IRDye78 injection (Fig. 3A; discussed below). Over the next 6 h, IRDye78 was eliminated by the genitourinary and biliary systems (Fig. 3A). Gallbladder filling and contraction and intestinal peristalsis were visible during this time (data not shown). By 6 h, NIR fluorescence had returned to near background except in the above sites of elimination (Fig. 3A).

Intravenous injection of Pam78 (Fig. 3B) resulted in similarly rapid distribution throughout the body and intense NIR fluorescence of the animal. However, as Pam78 was cleared, areas of osteoblastic activity became visible. As early as 15 min postinjection, Pam78 uptake in the spine, ribs, paws, and knees could be detected above background, and by 3 h, most bony structures were visible (Fig. 3B). Although a 500 ms exposure time was used throughout this study to match the full dynamic range of the camera, acquisition times as short as 50 ms resulted in excellent quality images, indicating that real-time dynamic NIR fluorescence imaging will be possible with newly introduced interlined NIR cameras.

Pharmacokinetics of IRDye78 and Pam78. IRDye78 (Fig. 3C) achieves peak concentration within 1 min after intravenous injection and exhibits a two-phase elimination from the plasma, with early and late half-lives of 7.2 and 24.7 min, respectively. The late *in vivo* half-life is consistent with the late *in vivo* half-lives reported for similar polysulfonated indocyanine NIR fluorophores[21]. Pam78 also shows peak plasma concentration by 1 min, with a more rapid clearance having early and late half-lives of 5.0 and 15.4 min, respectively.

Comparison of NIR fluorescence to radioscintigraphy. Optimal Pam78 images were obtained 6 h after injection (Fig. 4A, left and right panels). All of the dorsal bony structures delineated in Figure 3B became better defined, and ventral imaging revealed additional structures such as bones of the maxilla, sternum, and knees (Fig. 4A, right panel).

Before this study, the gold standard for imaging HA was a bone scan with ^{99m}Tc-MDP. To directly compare these two imaging methods, we re-injected the same animal shown in Figures 3B and 4A with ^{99m}Tc-MDP and imaged it by planar radioscintigraphy 6 h later (Fig. 4B). Because of the inherent trade-off between pinhole size and FOV, it was not possible to image the entire animal with higher resolution than that shown. Also, the radioscintigraphic image required a 30 min integration time for 0.4 mCi of ^{99m}Tc-MDP injected vs. a 500 ms image acquisition time for NIR fluorescence using 2.6 nmol of Pam78.

Effect of target depth on signal intensity. The correlation of anatomical landmarks imaged by MRI (Fig. 4C) with signal intensity (Fig. 4A) permits the modeling of observed NIR fluorescence signal as a function of target depth beneath the skin surface. In Figure 4D, the net NIR fluorescent signal intensities of the first seven visible spinous processes (Fig. 4A, left panel) were plotted against their depth beneath the surface of the skin as measured by MRI. The data fit an exponential decay curve where measured intensity is proportional to e^{kd}, $k = -0.43$/mm and d = distance from the skin surface to the target in millimeters (R^2 of fit = 0.98).

Quantitation of Pam78 skeletal uptake. Because the harsh conditions necessary for bone dissolution (6 N HCl) destroyed the fluorophore (data not shown), we estimated Pam78 uptake by measuring fluorescence intensity of the ribs in the skinless animal (Fig. 4A, middle panel). Calibration standards matching the geometry of the ribs were placed next to the animal, and mean fluorescence intensities of each standard and the caudal three ribs on each side were measured. Pam78 concentration (mean ± s.e.m.) was found to be 0.91 ± 0.027 µM. Assuming a bone density of 1.8 g/cm^3 (ref. 22) and a skeletal weight of 11.8% body weight[23], 1.5 nmol (57%), out of 2.6 nmol injected, bound to the skeleton. The skeletal uptake of Pam78 compares favorably with the 52% uptake reported in rats using ^{99m}Tc-MDP (ref. 24).

High-resolution *in vivo* NIR fluorescence imaging. The small-animal NIR fluorescence imaging system described above was designed to include zoom capability. Six hours after Pam78 injection, the same animal shown in Figures 3B and 4 was used to obtain high-resolution images of various sites of osteoblastic activity (Fig. 5). Although scatter from the skin and overlying soft tissue resulted in blurring of some structures, most bones of the animal could be visualized; some, like the bones of the maxilla, could be seen with extremely high clarity (discussed below).

Discussion

This study highlights many of the principles of NIR fluorescence imaging. Of paramount importance is the choice of fluorophore. The NIR window has a local minimum at ~800 nm, and fluorophores with excitation/emission wavelengths close to 800 nm should permit maximal photon penetration into living tissue[25]. IRDye78 and its derivatives have an excitation wavelength of 771 nm, emission wavelength of 796 nm, and a relatively high extinction coefficient and quantum efficiency. The NHS ester of

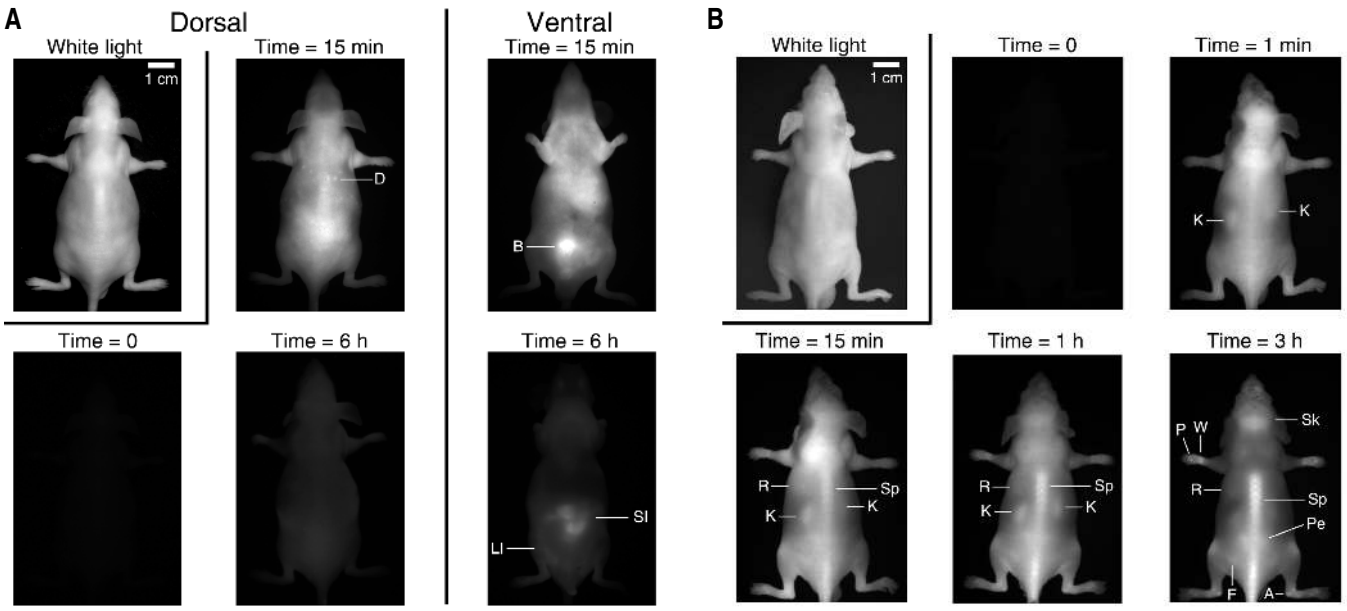

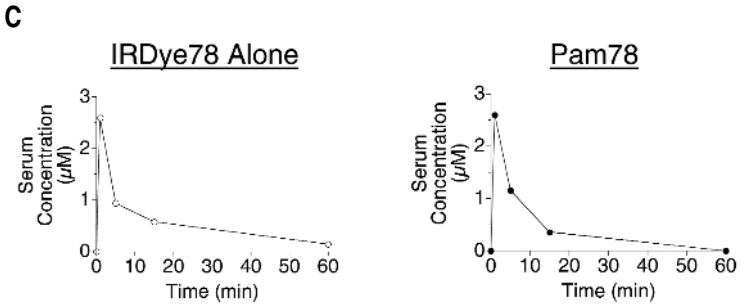

Figure 3. *In vivo* biodistribution and pharmacokinetics of IRDye78 and Pam78 using NIR fluorescence imaging. (A) 2.6 nmol of IRDye78 carboxylic acid in 80 μl of PBS were injected intravenously in the tail vein of a hairless (*nu*/*nu*) mouse and imaged with the small-animal imaging system. The left panels show dorsal images and the right panels show ventral images of the same mouse. A white-light image and calibration bar are shown in the panel at top left. All NIR fluorescence images were acquired using a 500 ms exposure time and are normalized to the 15 min dorsal image. The time = 0 photograph shows NIR autofluorescence before compound injection. Dorsal and ventral images at 15 min and 6 h post injection are shown. In the 15 min dorsal image, sub-millimeter skin defects, D, appear highlighted after injection. In the 15 min ventral image, note the intense signal in the bladder, B. In the 6 h ventral image, note the signal emanating from loops of the large (LI) and small (SI) intestine. (B) 2.6 nmol of Pam78 in 80 μl of PBS was injected intravenously in the tail vein of a hairless (*nu*/*nu*) mouse, and dorsal images were obtained with the small-animal imaging system. A white-light image and calibration bar are shown in the panel at top left. All NIR fluorescence images were acquired using a 500 ms exposure time and are normalized to the 6 h image of Figure 4A (left panel). The time = 0 image shows NIR autofluorescence before compound injection. As the injected fluorophore is cleared, areas of high HA in the skeleton become visible. As early as 15 min after injection, ribs, R, spine, Sp, and kidney, K, are visualized. By 3 h, the phalanges (P), wrist (W), skull (Sk), pelvis (Pe), femur (F), and ankle (A) become visible. (C) Serum concentration of IRDye78 carboxylic acid (left panel; open circles) and Pam78 (right panel; closed circles) were measured after intravenous injection of 2.6 nmol of each compound into the tail vein. Ordinate, serum concentration as measured spectrophotometrically. Abscissa, time in minutes.

IRDye78 permits one-step conjugation to primary-amine-containing ligands, and products can be purified by TLC. Polysulfonated indocyanines such as IRDye78 have extremely low toxicities[21], and plasma half-lives in the range of 10–30 min (this study; ref. 21) result in rapid clearance of background signal. Pam78 also appears to be stable *in vivo* considering that, even 12 h post injection, there is no degradation of skeletal signal (data not shown). This suggests that the amide bond between pamidronate and IRDye78, and the fluorophore itself, were not hydrolyzed significantly *in vivo*.

Pam78 provides a convenient reagent for creating "embedded targets" in a living animal. NIR fluorescence imaging systems are usually evaluated using fluorescent phantoms that seldom have relevance to *in vivo* imaging. Pam78, however, creates an essentially infinite number of target structures embedded at all depths within a living animal. Such a reagent should be valuable for creating the much-needed next generation of NIR fluorescence imaging systems.

By measuring the observed NIR fluorescence intensity as a function of optical path length between excitation light and target, we were able to derive the exponential decay constant of $k = -0.43$/mm (Fig. 4D). This model predicts that the presence of skin (0.89 mm thick on the back of a 25 g nude mouse; A. Zaheer and J.V. Frangioni, unpublished observations) would reduce net NIR fluorescence signal intensity by 32%. After adjusting for exposure time, comparison of the animal shown in Figure 4A with and without skin resulted in an intensity attenuation of 44%, in reasonable agreement with the model. This model may be useful as a frame of reference for investigators contemplating the use of NIR fluorescence for target detection *in vivo*. Of course, the presence of skin markedly reduces the quality of the image by causing scatter. As can be seen in Figure 4A, optical scatter is a major limitation to planar imaging using NIR light. The use of an optical coupling medium and/or tomographic imaging[26,27] may provide a means of minimizing this effect.

Pam78 has several immediate applications in the study of skeletal disease. It provides high-resolution imaging of HA without compromising sensitivity and specificity (Figs 3B, 4A, 5). Certain structures such as the bones of the maxilla (Fig. 5A) are seen with near-photographic clarity, which should permit detailed, noninvasive study of maxillofacial development. Skeletal development in higher (e.g., mouse, ref. 28; reviewed in ref. 29) and lower (e.g., zebra fish) vertebrates, as well as animal

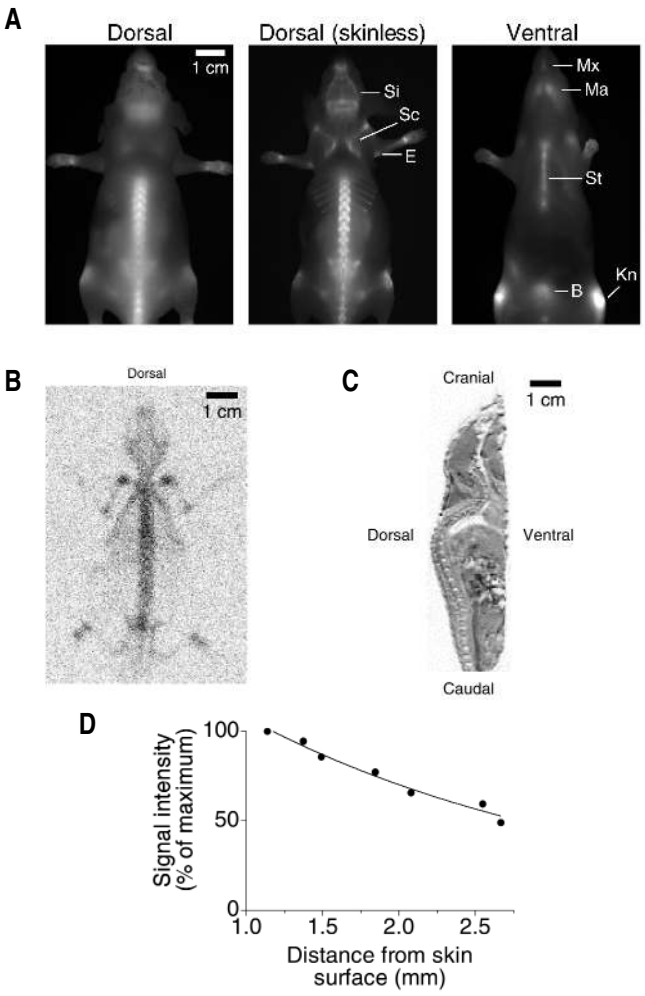

Figure 4. Direct comparison of *in vivo* NIR fluorescence imaging of HA to radioscintigraphic and MRI imaging in the same animal, and quantitation of NIR light attenuation by living tissue. (A) Dorsal (far left panel) and ventral (far right panel) of the same animal shown in Figure 3B imaged 6 h after injection of Pam78. Higher definition of all bony structures identified in Figure 3B can be seen in the dorsal image. The ventral image permits visualization of the maxilla (Mx), mandible (Ma), sternum (St), bladder (B), and knee (Kn). Middle panel, same animal, immediately after euthanasia, with the skin removed. The sinuses (Si), scapula (Sc), and elbow (E) now become visible, and all other bony structures are better resolved. The dorsal/skinless photograph (middle panel) was made in one-half the exposure time (i.e., 250 ms) of the images in Figures 3B and 4A so as to avoid pixel saturation. (B) Dorsal planar radioscintigraphic imaging of the same animal in Figures 3B, 4A, and 4B using a 1 mm tantalum pinhole, 6 h after injection of 0.4 mCi ^{99m}Tc-MDP. (C) Midline sagittal fast-gradient echo T1-weighted MRI of the same animal in Figures 3B,4A, and 4B. (D) Quantitation of net fluorescence signal as a function of target distance from the skin surface. MRI imaging was used to measure the distance between the skin surface and spinous processes of the animal shown in Figure 4A (left panel). At each spinous process the net NIR fluorescence signal was quantitated using IPLab software, permitting correlation of target depth with NIR fluorescence signal intensity.

models of bony disease[30,31], could be studied with this technology. Although the present study was conducted with hairless animals, chemical hair removal using commercially available products should permit any mouse strain to be used (A. Zaheer and J.V. Frangioni, unpublished observations).

Pathological skeletal processes such as osteoblastic metastases should also be readily detectable using this technology. Our comparison of radioscintigraphy with ^{99m}Tc-MDP and NIR fluorescence imaging showed there were distinct advantages to each method (Figs 3B, 4A–C). NIR fluorescence imaging was extremely rapid (≤500 ms for complete image acquisition and processing), had high sensitivity after only 2.6 nmol of injected Pam78, and offered relatively high spatial resolution (Fig. 5). However, deep structures were either poorly visualized or not visualized at all with our experimental apparatus as a result of skin and soft-tissue attenuation and scatter (Fig. 4A). In comparison, planar radioscintigraphy required long integration times, and a trade-off between FOV and spatial resolution. However, imaging of deep structures was possible because the 140 keV γ-ray is highly penetrant and minimally scattered. We propose that NIR fluorescence detection may permit the earliest genetic changes associated with osteoblastic metastases to be studied more easily in mouse model systems because small lesions can be detected rapidly, with high resolution, and nonisotopically in the living animal.

The technology described in this study may also have several nonskeletal applications. First, the carboxylic acid of IRDye78 spreads rapidly throughout the body and is able to highlight even small defects in the skin (Fig. 3A). It may be possible, therefore, to use IRDye78 as a part of a sensitive detection system for dermatological disease. Indeed, a related NIR fluorophore, indocyanine green, has already been used in such a manner[32,33]. Second, there are several effects of pamidronate, such as direct osteoclast inhibi-

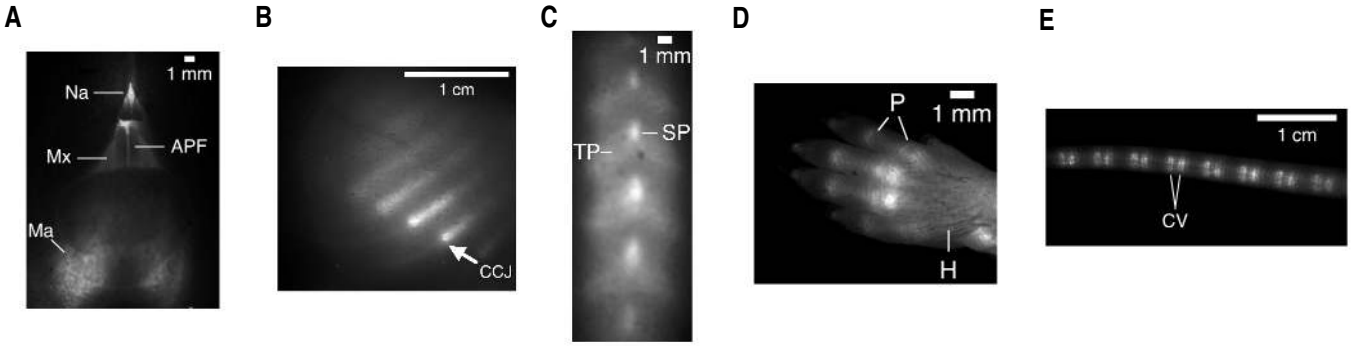

Figure 5. High-resolution *in vivo* NIR fluorescence imaging of HA. Specific anatomical sites of the same living animal shown in Figures 3B and 4A (left panel) were imaged 6 h post injection of Pam78 using the zoom lens capability of the small-animal imaging system. Images were normalized for optimal appearance of each bony structure. For orientation, calibration bars are shown in each photograph. (A) Ventral image of the head showing intense staining of the nasal bone (Na) and maxilla (Mx). The anterior palatine foramen (APF) is also visible, as is the (out of focus) mandible (Ma). (B) Oblique image of ribcage showing costochrondral junction (arrow; CCJ). (C) The thoracic spine showing spinous (SP) and transverse processes (TP). (D) The front paw showing individual phalanges (P). Note is made of small opaque hairs (H) near the wrist preventing penetration of NIR light. (E) The mid-tail showing caudal vertebrae (CV). Soft tissue and skin overlying these bones can be seen as a superimposed ribbed and checkered pattern.

tion[34] and parasite toxicity[35], which defy mechanistic explanation at present. Pam78 may be a valuable reagent to visualize the binding of pamidronate to osteoclasts and parasites in the hope of better defining its mechanism of action. Third, middle/inner ear anomalies caused by HA deposition, such as otosclerosis[36], could be detected with high sensitivity and specificity by injecting Pam78 intravenously, placing a fiberscope against the tympanic membrane, and directly visualizing NIR fluorescence.

Finally, this technology should be useful for imaging early manifestations of coronary calcification. Even ^{99m}Tc-MDP is capable of imaging aortic calcification[37], but only in advanced disease and with low resolution. Intravenous or intracoronary injection of Pam78 would be expected to highlight even microscopic HA deposits, because intimal thickness[38] is well within the range of this technology. In analogy to intravascular ultrasound, a NIR fluorescence angioscope inserted into a coronary artery should permit visualization of the earliest precursor lesions of vascular calcification and, hence, permit intervention before a conventional plaque forms. Indeed, if it is determined that the yield of triplet formation of Pam78 is sufficient, it may be possible to perform both detection (by fluorescence angioscopy) and treatment (by photodynamic therapy; ref. 39) of subclinical atherosclerotic lesions with this single compound.

Experimental protocol

Reagents. Pamidronate disodium was from Interchem Corporation (Paramus, NJ). NHS-IRDye78 was purchased from LI-COR (Lincoln, NE) and stored under nitrogen at –80°C. The carboxylic acid of IRDye78 was a generous gift from LI-COR. HA (catalog no. 391947) was from Calbiochem (La Jolla, CA), and Fluoromount-G was from Southern Biotechnology Associates (Birmingham, AL). All other chemicals were from Sigma (St. Louis, MO).

Conjugation and purification of Pam78. Pamidronate in H_2O was adjusted to pH 8.5 with 0.1 N NaOH. A 1 ml reaction involving 10 mM pamidronate and 5.5 mM IRDye78 NHS ester in H_2O was carried out in the dark. After 18 h at room temperature with constant motion, the bright-green reaction components were separated by TLC (Whatman LK6DF), without using the preabsorbent layer. Mobile phase was 65% acetonitrile/35% H_2O. Unconjugated pamidronate was visualized with 0.25% ninhydrin in acetone and heat. After scraping, product was eluted with 20% acetonitrile/80% H_2O, filtered (model UFC3-0GV-25, Millipore, Bedford, MA), lyophilized, resuspended in H_2O, refiltered, and stored in the dark at –80°C until use. Yield was calculated using $\varepsilon_{771\,nm}$ = 150,000 M/cm.

Spectral measurements. Absorbance was measured on a Model DU-600 spectrophotometer (Beckman, Fullerton, CA) using 1 μM of each compound in 20 mM *N*-ethylmorpholine, pH 7.4, and 150 mM KCl (NK buffer). Fluorescence was measured on a SPECTRAmax Gemini XS microplate reader (Molecular Devices, Sunnyvale, CA) using model 655076 black 96-well plates (Greiner, Lake Mary, FL), and 500 nM of each compound in NK buffer.

***In vitro* HA-binding experiments.** For kinetic measurements, 5 μM final Pam78 or the carboxylic acid of IRDye78 in 100 μl NK buffer containing 1.5 mg/ml (1.5 mM) HA was continuously vortexed at 37°C. Unbound material was separated using a 0.2 μm filter (model MAGVN2210; Millipore), and the concentration of filtrate measured optically. Bound material was calculated by subtracting unbound from total. For steady-state binding, the indicated concentration of compound was incubated in 100 μl NK buffer containing 1.5 mg/ml (1.5 mM) HA. Suspensions were continuously vortexed at 37°C for 3 h and processed as above. For competition experiments, free pamidronate was pre-incubated in 100 μl NK buffer with 1.5 mg/ml (1.5 mM) HA for 5 min at room temperature with continuous vortexing, Pam78 was added to 2.5 μM final for 3 h, and binding was measured as above.

For NIR fluorescence imaging of HA crystals, 1 μM of indicated compound in 100 μl NK buffer was incubated with 1.5 mg/ml (1.5 mM) HA for 15 min at room temperature with continuous vortexing. Crystals were washed 3× with NK buffer, resuspended in Fluoromount-G, and mounted on glass slides.

NIR fluorescence microscopy. NIR fluorescence images were acquired on a Nikon Eclipse TE-300 epi-fluorescence microscope equipped with a 100 W mercury light source, NIR-compatible optics, and a NIR-compatible 10× PlanFluor objective lens (model 93171; Nikon, Melville, NY). A custom IRDye78 filter set (Chroma Technology Corporation, Brattleboro, VT) was composed of a 750 ± 25 nm excitation filter, a 785 nm dichroic mirror, and an 810 ± 20 nm emission filter. Images were acquired on a Photometrics Sensys charge-coupled device (CCD) camera (model 1401; Roper Scientific, Tucson, AZ) with heat filter removed. Image acquisition and analysis was performed using IPLab software (Scanalytics, Fairfax, VA).

Small-animal *in vivo* NIR fluorescence imaging system. The system consisted of two 150 W halogen light sources (model PL-900, Dolan-Jenner, Lawrence, MA) to which were mounted light guides (model BXS-236) and excitation filters (see above). Emitted light passed through the above emission filter and was collected using a Macrovideo zoom lens with detachable close-up lens (Optem, Fairport, NY), into the Sensys camera. Image acquisition, typically 250–500 ms with camera gain of 2, was controlled by IPLab. Excitation power density was measured using a calibrated thermopile detector (model 2M) and 1000 V/V pre-amplifier (model 1010; both from Laser Components, Santa Rosa, CA).

Compound injection and measurement of serum concentration. Hairless seven-week-old male *nu/nu* mice (Charles River Laboratories, Wilmington, MA; average weight 25 g) were anesthetized intraperitoneally with 50 mg/kg pentobarbital. The lateral tail vein was injected with 2.6 nmol of compound in 80 μl of PBS. To measure plasma concentration, 75 μl of whole blood was collected in a capillary tube by milking of the tail vein, and clotted cells removed by centrifugation. Serum was diluted 1:10 in 50 mM HEPES, pH 7.4, and an absorbance scan from 400 nm to 850 nm was performed. Serum concentration was determined by peak height at 771 nm after subtraction of background (pre-injection serum), and correction for hemoglobin absorbance.

MRI. Anesthetized animals were placed in a custom low-pass birdcage coil (10 cm length, 6 cm diameter) and imaged with a 3 T whole-body scanner (General Electric Medical Systems, Waukesha, WI). Images were acquired with an 8 cm FOV using a 3-D fast gradient echo sequence. Other parameters included a 256 × 256 pixel matrix size, slice thickness of 0.7 mm, TE= 2.6 ms, T*R* = 10.2 ms, and flip angle = 15 degrees.

Planar ^{99m}Tc-MDP radioscintigraphy. Anesthetized animals were injected with 0.4 mCi ^{99m}Tc-MDP and imaged 6 h later. Dorsal images in a 512 × 512 pixel format were integrated for a total of 30 min through a custom 1 mm tantalum pinhole mounted on a Forte gamma camera (ADAC Laboratories, Milpitas, CA).

Acknowledgments

We thank Daniel S. Kemp and Stephan D. Voss for helpful discussions, and Alec DeGrand, Ananda Lugade, Christopher Mantzios, Kerry Petersen, Daniel Draney, Michelle Pastore, Alice Carmel, David Lee-Parritz, Angeline Warner, Stephen Moore, J. Anthony Parker, Rachel Katz-Brull, Barry Alpert, Victor Laronga, Michael Paszak, Patrick Verdier, Paul Nothnagle, Paul Millman, Kenneth Wilson, Victor Yen, Maxx Abraham, and Fernando Delaville for technical assistance. We thank Rebekah Taube for proofreading and Grisel Rivera for administrative assistance. A.Z. is a Radiology Training Grant Fellow of the National Cancer Institute (NCI). A.M. and A.G.J. acknowledge support from US Public Health Service (US PHS) grant R01CA/34970. J.V.F. is supported by the Howard Hughes Medical Institute, Doris Duke Charitable Foundation (nonanimal experiments), Paul D. and Lovie S. Kemp Career Development Fund for Prostate Cancer, the Hershey Family Foundation, the Rita Leabman Memorial Fund, and a grant from the NCI (R21CA88245).

Received 20 June 2001; accepted 28 September 2001

1. Marks, S.C. & Popoff, S.N. Bone cell biology: the regulation of development, structure, and function in the skeleton. *Am. J. Anat.* **183**, 1–44 (1988).
2. Jakoby, M.G. & Semenkovich, C.F. The role of osteoprogenitors in vascular calcification. *Curr. Opin. Nephrol. Hypertens.* **9**, 11–15 (2000).
3. Watson, K.E. Pathophysiology of coronary calcification. *J. Cardiovasc. Risk* **7**, 93–97 (2000).
4. Jung, A., Bisaz, S. & Fleisch, H. The binding of pyrophosphate and two diphosphonates by hydroxyapatite crystals. *Calcif. Tissue Res.* **11**, 269–280 (1973).
5. Fleisch, H. Bisphosphonates—history and experimental basis. *Bone* (Suppl. 1) **8**, S23–S28 (1987).
6. Altkorn, D. & Vokes, T. Treatment of postmenopausal osteoporosis. *JAMA* **285**, 1415–1418 (2001).
7. Eastell, R. Treatment of postmenopausal osteoporosis. *N. Engl. J. Med.* **338**, 736–746 (1998).
8. Mundy, G.R. & Yoneda, T. Bisphosphonates as anticancer drugs. *N. Engl. J. Med.* **339**, 398–400 (1998).
9. Klenner, T., Wingen, F., Keppler, B.K., Krempien, B. & Schmahl, D. Anticancer-agent-linked phosphonates with antiosteolytic and antineoplastic properties: a promising perspective in the treatment of bone-related malignancies? *J. Cancer Res. Clin. Oncol.* **116**, 341–350 (1990).
10. Fujisaki, J. *et al.* Osteotropic drug delivery system (ODDS) based on bisphosphonic prodrug. I: synthesis and *in vivo* characterization of osteotropic carboxyfluorescein. *J. Drug Target.* **3**, 273–282 (1995).
11. Fujisaki, J. *et al.* Physicochemical characterization of bisphosphonic carboxyfluorescein for osteotropic drug delivery. *J. Pharm. Pharmacol.* **48**, 798–800 (1996).
12. Fujisaki, J. *et al.* Osteotropic drug delivery system (ODDS) based on bisphosphonic prodrug. III: Pharmacokinetics and targeting characteristics of osteotropic carboxyfluorescein. *J. Drug Target.* **4**, 117–123 (1996).
13. Fujisaki, J. *et al.* Osteotropic drug delivery system (ODDS) based on bisphosphonic prodrug. V. Biological disposition and targeting characteristics of osteotropic estradiol. *Biol. Pharm. Bull.* **20**, 1183–1187 (1997).
14. Fujisaki, J. *et al.* Osteotropic drug delivery system (ODDS) based on bisphosphonic prodrug. IV. Effects of osteotropic estradiol on bone mineral density and uterine weight in ovariectomized rats. *J. Drug Target.* **5**, 129–138 (1998).
15. Hirabayashi, H. *et al.* Bone-specific delivery and sustained release of diclofenac, a non-steroidal anti-inflammatory drug, via bisphosphonic prodrug based on the Osteotropic Drug Delivery System (ODDS). *J. Control. Release* **70**, 183–191 (2001).
16. Bachman, C.H. & Ellis, E.H. Fluorescence of bone. *Nature* **206**, 1328–1331 (1965).
17. Prentice, A.I. Autofluorescence of bone tissues. *J. Clin. Pathol.* **20**, 717–719 (1967).
18. Chance, B. Near-infrared images using continuous, phase-modulated, and pulsed light with quantitation of blood and blood oxygenation. *Ann. N.Y. Acad. Sci.* **838**, 29–45 (1998).
19. Lin, J.H., Duggan, D.E., Chen, I.W. & Ellsworth, R.L. Physiological disposition of alendronate, a potent anti-osteolytic bisphosphonate, in laboratory animals. *Drug Metab. Dispos.* **19**, 926–932 (1991).
20. Mahmood, U., Tung, C.H., Bogdanov, A. & Weissleder, R. Near-infrared optical imaging of protease activity for tumor detection. *Radiology* **213**, 866–870 (1999).
21. Miwa, N. *et al.* In Patent Cooperation Treaty WO 00/16810 (2000).
22. Reilly, D.T. & Burstein, A.H. The elastic and ultimate properties of compact bone tissue. *J. Biomech.* **8**, 393–405 (1975).
23. McKern, N.M. Comparison of skeletal growth in normal and "little" mice. *Growth* **46**, 53–59 (1982).
24. Cleynhens, B. *et al.* ^{99m}Tc-bone agents with rapid renal excretion. In *Technetium, rhenium and other metals in chemistry and nuclear medicine.* (eds Nicolini, M. & Mazzi, U.) 611–614 (Servizi Grafici Editoriali, Padova, Italy; 1999).
25. Quaresima, V., Matcher, S.J. & Ferrari, M. Identification and quantification of intrinsic optical contrast for near-infrared mammography. *Photochem. Photobiol.* **67**, 4–14 (1998).
26. Farkas, D.L. *et al.* Non-invasive image acquisition and advanced processing in optical bioimaging. *Comput. Med. Imaging Graph.* **22**, 89–102 (1998).
27. Ntziachristos, V., Yodh, A.G., Schnall, M. & Chance, B. Concurrent MRI and diffuse optical tomography of breast after indocyanine green enhancement. *Proc. Natl. Acad. Sci. USA* **97**, 2767–2772 (2000).
28. Sabatakos, G. *et al.* Overexpression of DeltaFosB transcription factor(s) increases bone formation and inhibits adipogenesis. *Nat. Med.* **6**, 985–990 (2000).
29. Olsen, B.R., Reginato, A.M. & Wang, W. Bone development. *Annu. Rev. Cell. Dev. Biol.* **16**, 191–220 (2000).
30. Gunther, T. & Schinke, T. Mouse genetics have uncovered new paradigms in bone biology. *Trends Endocrinol. Metab.* **11**, 189–193 (2000).
31. Drake, W.M., Kendler, D.L. & Brown, J.P. Consensus statement on the modern therapy of Paget's disease of bone from a Western Osteoporosis Alliance symposium. *Clin. Ther.* **23**, 620–626 (2001).
32. Karrer, S. *et al.* Photochemotherapy with indocyanine green in cutaneous metastases of rectal carcinoma (in German). *Dtsch. Med. Wochenschr.* **122**, 1111–1114 (1997).
33. Abels, C. *et al.* Indocyanine green (ICG) and laser irradiation induce photooxidation. *Arch. Dermatol. Res.* **292**, 404–411 (2000).
34. Rogers, M.J. *et al.* Cellular and molecular mechanisms of action of bisphosphonates. *Cancer* **88**, 2961–2978 (2000).
35. Martin, M.B. *et al.* Bisphosphonates inhibit the growth of Trypanosoma brucei, Trypanosoma cruzi, Leishmania donovani, Toxoplasma gondii, and Plasmodium falciparum: a potential route to chemotherapy. J. Med. Chem. **44**, 909–916 (2001).
36. Lim, D.J. & Saunders, W.H. Otosclerotic stapes: morphological and microchemical correlates. An electron microscopic and x-ray analytical investigation. *Ann. Otol. Rhinol. Laryngol.* **86**, 525–540 (1977).
37. Ikehira, H., Furuichi, Y., Kinjo, M., Yamamoto, Y. & Aoki, T. Multiple extra-bone accumulations of technetium-99m-HMDP. *J. Nucl. Med. Technol.* **27**, 41–42 (1999).
38. Dupouy, P., Geschwind, H.J., Pelle, G., Gallot, D. & Dubois-Rande, J.L. Assessment of coronary vasomotion by intracoronary ultrasound. *Am. Heart J.* **126**, 76–85 (1993).
39. Rockson, S.G. *et al.* Photoangioplasty for human peripheral atherosclerosis: results of a phase I trial of photodynamic therapy with motexafin lutetium (Antrin). *Circulation* **102**, 2322–2324 (2000).